

Prediction of load transfer depth for cost-effective design of ground anchors using FBG sensors embedded tendon and numerical analysis

Tan Manh Do^a and Young-Sang Kim^{*}

Department of Civil and Environmental Engineering, Chonnam National University, Yeosu 59626, Korea

(Received July 7, 2015, Revised February 25, 2016, Accepted February 29, 2016)

Abstract. The load transfer depth of a ground anchor is the minimum length required to transfer the initial prestressing to the grout column through the bonded part. A thorough understanding of the mechanism of load transfer as well as accurate prediction of the load transfer depth are essential for designing an anchorage that has an adequate factor of safety and satisfies implicit economic criteria. In the current research, experimental and numerical studies were conducted to investigate the load transfer mechanism of ground anchors based on a series of laboratory and field load tests. Optical FBG sensors embedded in the central king cable of a seven-wire strand were successfully employed to monitor the changes in tensile force and its distribution along the tendons. Moreover, results from laboratory and in-situ pullout tests were compared with those from equivalent case studies simulated using the finite difference method in the FLAC 3D program. All the results obtained from the two proposed methods were remarkably consistent with respect to the load increments. They were similar not only in trend but also in magnitude and showed more consistency at higher pullout loading stages, especially the final loading stage. Furthermore, the estimated load transfer depth demonstrated a pronounced dependency on the surrounding ground condition, being shorter in hard ground conditions and longer in weaker ones. Finally, considering the safety factor and cost-effective design, the required bonded length of a ground anchor was formulated in terms of the load transfer depth.

Keywords: ground anchors; laboratory and field tests; FBG sensors; numerical analysis; load transfer depth

1. Introduction

As a result of less expensive and faster build systems, anchorage technology and practice have progressively evolved to become a feasible interdisciplinary technique used in almost every part of the world. Anchors, systematically installed in both rock and soil, enhance civil engineering works, in which it is essential to support, stabilize, and transfer applied loads acting on a wide spectrum of structures, foundations, and slopes.

A ground anchor, which functions as a load-bearing element, consists essentially of a steel tendon or strand tendon inserted into suitable ground formations in almost any direction and is used to transmit an applied tensile load to the soil or rock through a cement grout. A thorough

^{*}Corresponding author, Professor, E-mail: geoyskim@jnu.ac.kr

^a Ph.D. Student, E-mail: domanhtan@khoaxaydung.edu.vn

understanding of the mechanism of load transfer as well as accurate prediction of the load transfer depth are essential for designing an anchorage that has an adequate factor of safety and satisfies implicit economic criteria (Xanthakos 1991). Thus, there have been a number of studies addressing this problem using various approaches. Among these, Shields *et al.* (1978) successfully investigated the load transfer in pressure-injected anchors by using strain gauges and formulated relationships between load transfer (slope of the load distribution curve) and anchor displacement from the strain gauge data. In their results, the concentration of load transfer near the front of the anchor resulted from the dependence of load transfer mobilization on anchor displacement. During unloading, residual loads (and strains) were locked into the anchor by a shear stress reversal near the front of the anchor. The majority of this load redistribution was in response to strains induced in the soil mass by excavation, rather than by relaxation in the soil–anchor system. Benmokrane *et al.* (1995) monitored the behavior of grouted anchors using vibrating-wire gauges. A series of vibrating-wire gauges were micro-welded on the anchors at certain intervals along their lengths, and the performance of these gauges as well as the load transfer mechanism, debonding process, creep behavior, and long-term performance of the anchors under loading, unloading, and sustained loading were investigated in the laboratory. Moreover, a practical application of an instrumented anchor at Jeffrey Mine in Asbestos, Canada, was evaluated, and the test results showed that the instrumentation technique was efficient for long-term monitoring of grouted anchors. Kim *et al.* (2007a, 2008, 2009, 2011) ideally proposed a monitoring methodology for the tension force and load transfer in ground anchors using a smart tendon, which is a specially designed tendon proposed by embedding an FBG sensor into the center king cable of a 7-wire strand. The prestress forces measured by these smart tendons using the FBG sensors were found to be comparable with those measured by a conventional load cell. Other studies by Cornelia *et al.* (2003), Kesavan *et al.* (2005), Lee *et al.* (2004), Schroeck *et al.* (2000) and Moerman *et al.* (2005) were also used FBG sensors in the measurement. In the study by Aliciuc and Musat (2013), the test fields were simulated using the finite element method (FEM) for several types of soil models, taking into consideration the time factor. The displacement of a fixed length of a ground anchor was calculated for each soil model and compared with the measured displacement of the tested ground anchor.

The literatures reviewed above have provided insight into the load transfer of ground anchors by either experimental studies or numerical analysis. However, few studies have utilized both these methods simultaneously. Kim *et al.* (2007b) analyzed the load transfer of tension and compression anchors in weathered soil and performed numerical simulations of ground anchors. A procedure for finite element modeling and beam-column modeling of ground anchors was proposed in their study to investigate the load transfer mechanism in ground anchors. The procedure included the modeling of soil, grout, and strand tendon and the interface modeling of soil–grout and grout–strand in ground anchors. A series of finite element and beam-column analyses were performed on ground anchors using the proposed models, and the numerical results were compared with observed measurements in a field load test. The results indicated that the proposed numerical simulation of the load transfer mechanism in ground anchors could provide reasonable predictions. Chang *et al.* (2008) carried out in-situ pullout load tests on two prestressed anchors and found the failure signals to be comparable with those from a 2D/3D finite element modeling using ABAQUS. It was demonstrated that the analytical model could closely capture the progressive failures of the ground anchor with rational controls of the material strength parameters. Ivanovic and Neilson (2009) studied the debonding of a fixed length of ground anchorage, concentrating on the failure behavior of the bond at the proximal end of the fixed length. A

simulation of the anchorage system incorporating these bond models showed both a change in load distribution and a drop in the first natural frequency due to debonding. Moreover, a case study was simulated using the model, and the results showed good agreement with measured field data. In order to investigate the load transfer mechanism of ground anchors, Kim *et al.* (2013) conducted a series of field experiments and numerical modeling. The observed measurements from the in-situ load tests were compared with equivalent case studies simulated using the finite difference method in the FLAC 3D program. There was a good agreement between the experimental and numerical results.

In this study, a series of laboratory and in-situ pullout tests were performed using FBG sensors, and the results were quantitatively compared with equivalent case studies simulated using the finite difference method in the FLAC 3D program. Subsequently, with regard to safety factor, cost-effective design, and economic criteria, an expression for the required bonded length of the anchor was proposed in terms of the load transfer depth.

2. FBG embedded tendon with proper encapsulation technique

A fiber Bragg grating (FBG) is a type of distributed Bragg reflector constructed with a short segment of optical fiber that reflects particular wavelengths of light and transmits all others. This is achieved by creating a periodic variation in the refractive index of the fiber core, which generates a wavelength-specific dielectric mirror. An FBG can therefore be used as an inline optical filter to block certain wavelengths or as a wavelength-specific reflector (Gupta 2006).

Ideally, the optical fiber with Bragg grating (BG) sensors is encapsulated in a seven-wire strand as shown in Fig. 1. This takes advantage of the fact that the central steel wire of the seven-wire strand, called the “king wire,” is straight, whereas the other six wires wrap the king wire helically. In order to encapsulate the FBG sensor in the tendon, we developed the technique of replacing the king wire with a steel tube, in which the optical fiber with the FBG sensors is embedded. As the diameter of a typical optical fiber is approximately 0.25 mm, a steel tube with an internal diameter of 2.0 mm or less would be sufficiently large to accommodate the fiber and a low-viscosity liquid glue such as epoxy resin. Fig. 2 shows a cross section of the tendon including a tube with a diameter of 5.24 mm and an internal diameter of 1.0–2.0 mm. The steel tube can be easily manufactured by the pultrusion process, and the manufacturer working on the project is currently capable of extending its length up to 34.0 m. The tube is usually made of mild steel for easier pultrusion, and it is heat-treated to achieve a higher tensile strength of the prestressing tendon.

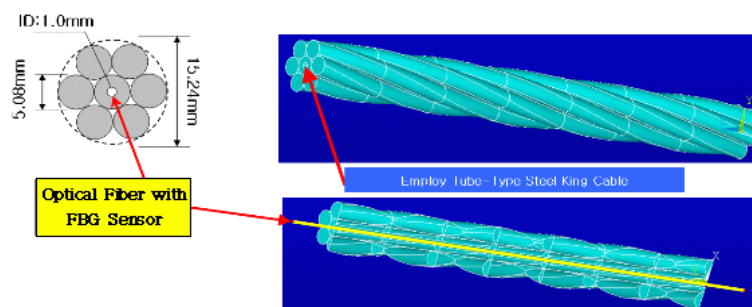


Fig. 1 Concept of smart tendon with FBG sensors

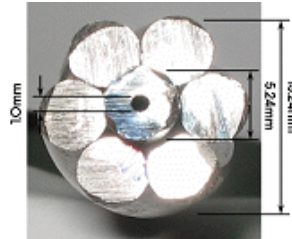


Fig. 2 A cross-section of real smart tendon

Currently, the yield strength of the tube is typically 50% of the wire in the prestressing tendon, whereas that of mild steel is approximately one-third of the high-strength wire. The strength of the tube is expected to be improved further in the near future (Kim *et al.* 2011). In this study, pullout tests were performed in the laboratory and the field to monitor the load transfer mechanism of anchors around the proposed smart tendons.

3. Experimental tests and results

3.1 Experimental procedure

The laboratory and field tests were performed sequentially in this study. For the laboratory pullout test, a 1 m long smart tendon in which five FBG sensors were embedded at different positions was used. The details of the test anchor with the locations and initial reflection wavelengths of the FBGs and the pullout test setup of the model anchor are schematically illustrated in Fig. 3. Herein, initial reflection wavelength is the wavelength of reflected light of FBG sensor before the pullout load is applied. The tendon was fixed to the model rock body with grout to replicate the installation conditions of the ground anchor. An Interrogator unit of Welltech Instrument Co. Ltd. was used to monitor the change in reflected wavelength due to strain variation.

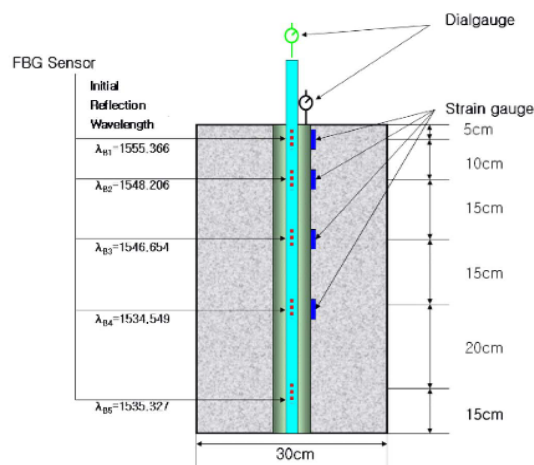


Fig. 3 Locations and initial reflection wavelengths of FBGs and pullout test setup of model anchor

A static pullout test with the loading system was performed with six increments of load, which was applied on top of the test anchor using a hydraulic jack and measured by a linear variable differential transformer (LVDT).

For the field tests, tension-type anchors were systematically installed in various ground conditions, such as weathered granite soil, weathered rock, normal rock, and hard rock, for the verification of the tension force monitoring of ground anchors at two different construction sites; one was located in the Yeosu area and the other at the Gimpo site. At the Yeosu site, the subsoil is composed of 4.3 m weathered soil (SM), a 2.7 m layer of weathered rock, normal rock, and a 5.8 m layer of hard rock, whereas at Gimpo site, there is a 2.4 m layer of soil (CL), 8.1 m layer of sand (SM), and weathered rock. The pullout test setup for measuring of pre-stress force and load transfer at construction sites is shown in Fig. 4. The ground conditions are shown in Fig. 5. Three 11.5 m long prototype anchors, designated A₁, A₂, and A₃, were fabricated by Sam Woo Geotechnical Co. Ltd., a leading company in the production of anchors in Korea.



Fig. 4 Pullout test setup for measuring of pre-stress force and load transfer at construction sites

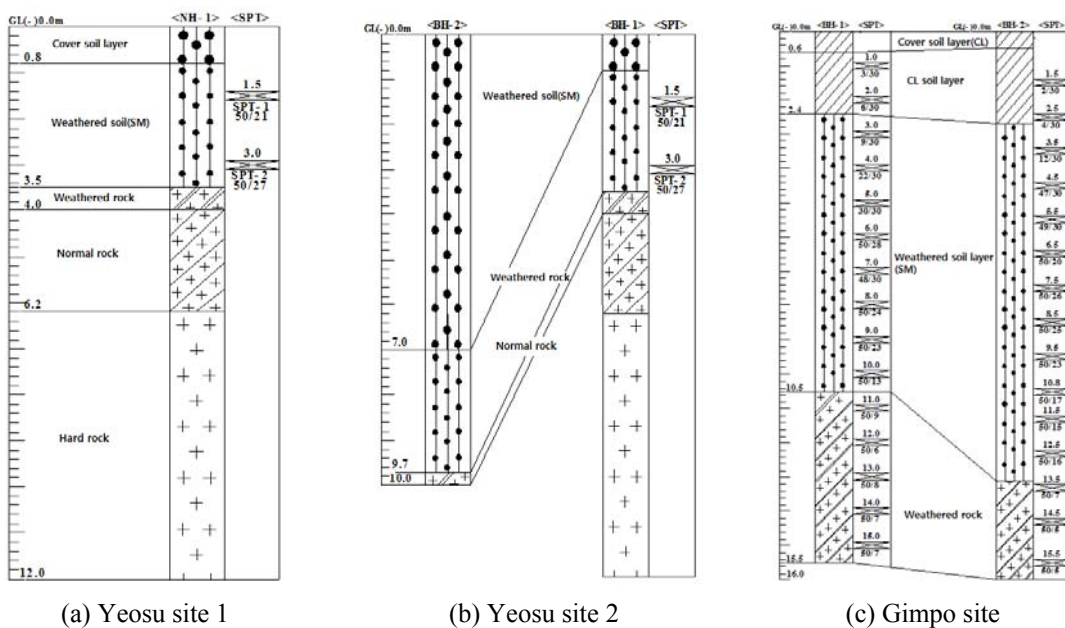


Fig. 5 Ground condition at different construction sites

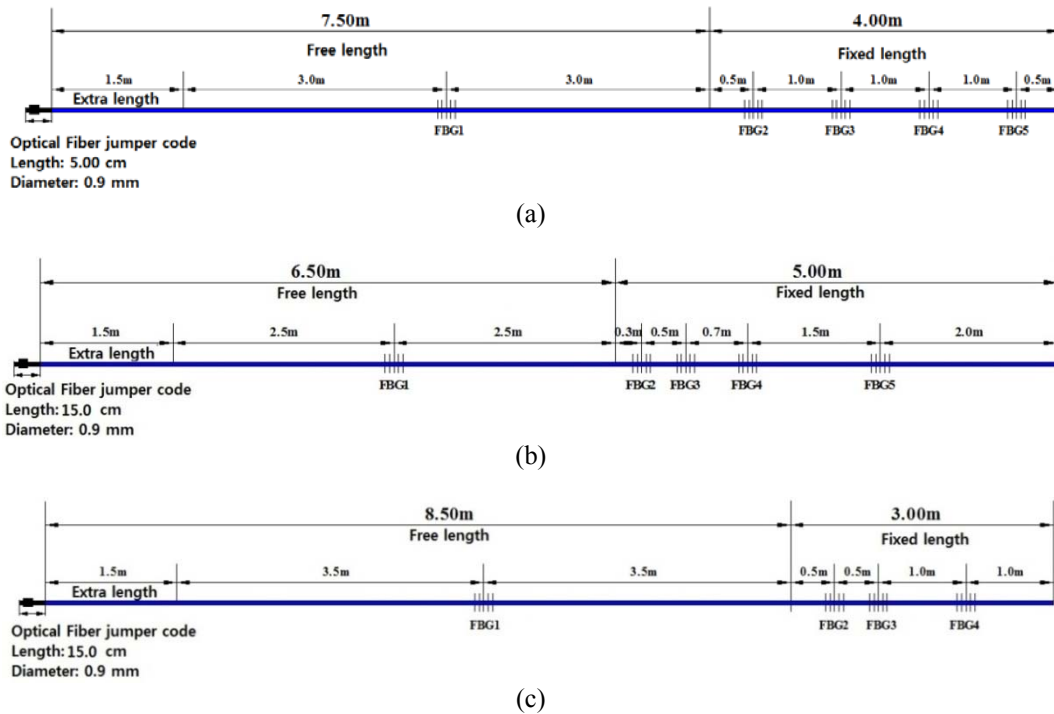


Fig. 6 Arrangement of FBG sensors embedded ground anchors: (a) Anchor A_1 ; (b) Anchor A_2 ; (c) Anchor A_3

Table 1 Dimensions of anchors and design conditions for pullout test

No	Anchor length (m)	Free length (m)	Fixed length (m)	Boring depth (m)	Boring diameter (mm)
A_1	11.5	7.5	4	10.5	105
A_2	11.5	6.5	5	10.5	105
A_3	11.5	8.5	3	10.5	105

Anchors A_1 and A_2 were installed at two different sites in the Yeosu area, and the bonded parts of the anchors were fixed in hard rock and normal rock, respectively. Anchor A_3 was installed at the Gimpo site, where the bonded-length parts were surrounded by hard soil and weathered rock. All the anchors were manufactured with the same dimensions but with different bonded lengths used in geotechnical practice. For the anchors A_1 and A_2 installed in the Yeosu site, the lengths of the bonded parts were 4.0 m and 5.0 m, respectively, whereas anchor A_3 was designed with a 3.0 m bonded length. The dimensions of the three anchors and the design conditions for the pullout tests are summarized in Table 1. The schematic arrangement of FBG sensors embedded ground anchors is shown in Fig. 6.

3.2 Laboratory test results

The strains were measured at each loading increment from the wavelength shift of the five FBG sensors. The strain distribution along the tendon measured by the FBG sensors is depicted in Fig. 7,

and it can be seen that it is essentially non-uniform and non-constant at each loading stage, as observed by previous researchers. At a load of 54.14 kN, the strain was transmitted from the proximal section but was not adequately significant. Then, it gradually decreased and almost possibly dissipated at the distal section. Therefore, only the proximal section was mobilized to resist the applied load at the small loading stage. For the load increments of 69.81 kN, 90.45 kN, 108.83 kN, 120.35 kN, and 150.92 kN, the corresponding strain distributions can be seen in Fig. 7 and a relative increase in strain can be observed at each loading stage. In particular, the strain was 2000 $\mu\epsilon$ at the applied load of 69.81 kN but reached around of 5400 $\mu\epsilon$ in the final loading stage. Therefore, it can be said that the strains gradually increase with respect to the load increment. Thus, in order to resist the large prestress force, the applied prestress force was transferred from the proximal part of the anchor interface to the distal part of the anchor.

$$\tau_{t-g} = \frac{E_t r_t}{2d} d\epsilon \tag{1}$$

where

- τ_{t-g} : Shear stress at the tendon-grout interface;
- r_t : Radius of tendon;
- E_t : Elastic modulus of tendon and elastic of grout;

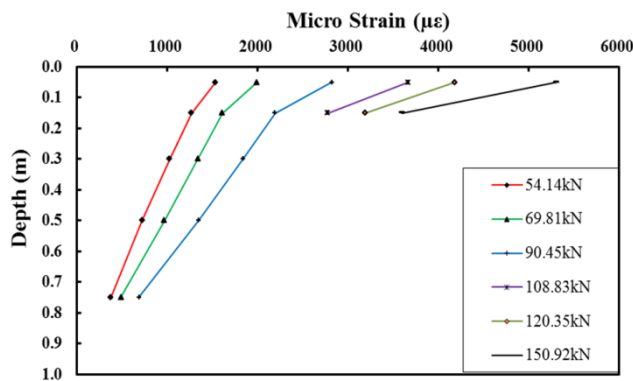


Fig. 7 Strain distribution along tendon measured by FBG sensors

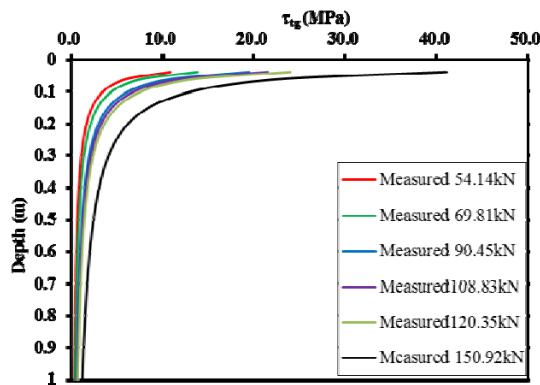


Fig. 8 Shear stress distributions at the interface of tendon and grout

- d : Distance between two measured points;
 d_ϵ : Difference in strain measured at the two points.

The shear stress distribution at the tendon–grout interface during successive stages of the pullout test can be seen in Fig. 8. The progressive evaluation of the shear stress is based on the measured strain as shown in Eq. (1) based on Farmer (1975) and Aydan *et al.* (1993, 1995). As the pull load increases, the bulk of the bond resistance begins to move toward the distal end until the final loading stage; in other words, the load transfer depth increases with the load increment.

3.3 Field test results

At the free part in which the tendon was not fixed to the surrounding ground, the first FBG sensor was located to directly measure the strain, and therefore the prestress force. Fig. 9 shows the wavelength shift of 1524.5 nm measured by the FBG sensor for the initial pullout force.

After the pullout load was applied, the wavelength continuously fluctuated with respect to time and finally reached the maximum value of 1532.20 nm. This result was used to determine the initial

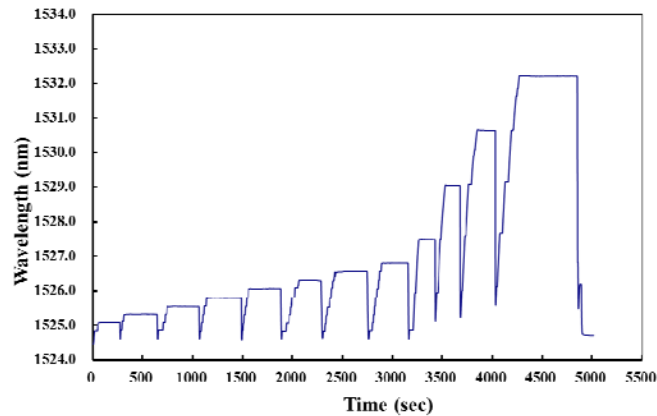


Fig. 9 Wavelength shift data measured from the first FBG sensor of anchor A_1

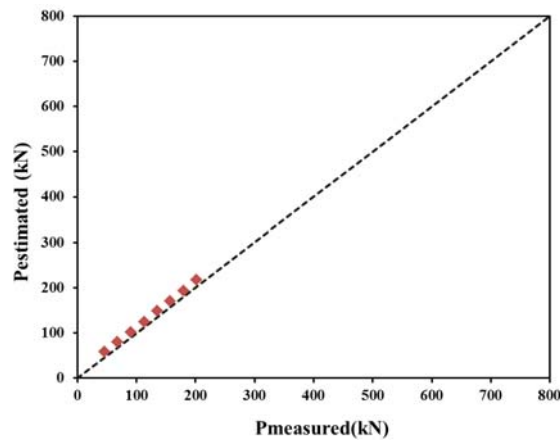


Fig. 10 Correlated measurement between FBG sensors and load cell of anchor A_1

pullout force, which was then compared with the measurement from a load cell, as shown in Fig. 10. A good agreement can be seen between the initial pullout force measured by the load cell and the prestress force estimated from the measurement of wavelength shift using the first FBG sensor in the smart tendon. Thus, the feasibility of the FBG sensors for monitoring the load transfer mechanism of the bonded parts was verified. For all the anchors, the FBG sensors located at the fixed and free lengths functioned properly during the monitoring period. The variation of tensile force with depth was obtained at each loading stage by multiplying the axial stiffness and the strain measured by the FBG sensors embedded in the anchor, as shown in equation (2). Consequently, the distributions of the introduced prestress force and the transfer of the prestress force from the proximal parts to the distal parts are depicted in Figs. 11(a), (b) and (c) for anchors A₁, A₂, and A₃, respectively.

$$P_{FBG} = N \times A_t \times E_t \times \varepsilon_{FBG} \tag{2}$$

where

- P_{FBG} : Prestress force determined based on the strain measured from the FBG sensor;
- N : Number of tendons in ground anchor;
- E_t : Young's modulus of the tendon;
- A_t : Effective cross-sectional area of the tendon;
- ε_{FBG} : Strain measured from the FBG sensors.

Anchor A₁ was installed at the Yeosu site with a 4 m fixed length surrounded by hard rock. It can be seen from Fig. 11(a) that the tensile force of anchor A₁ remained constant at the free part before dropping to zero at the distal end of the fixed length, for most of the loading stages. Moreover, the tensile force distribution along the bonded length was non-linear at each loading stage. At the first stage of 46.19 kN, the moderately small tensile force was transmitted from the

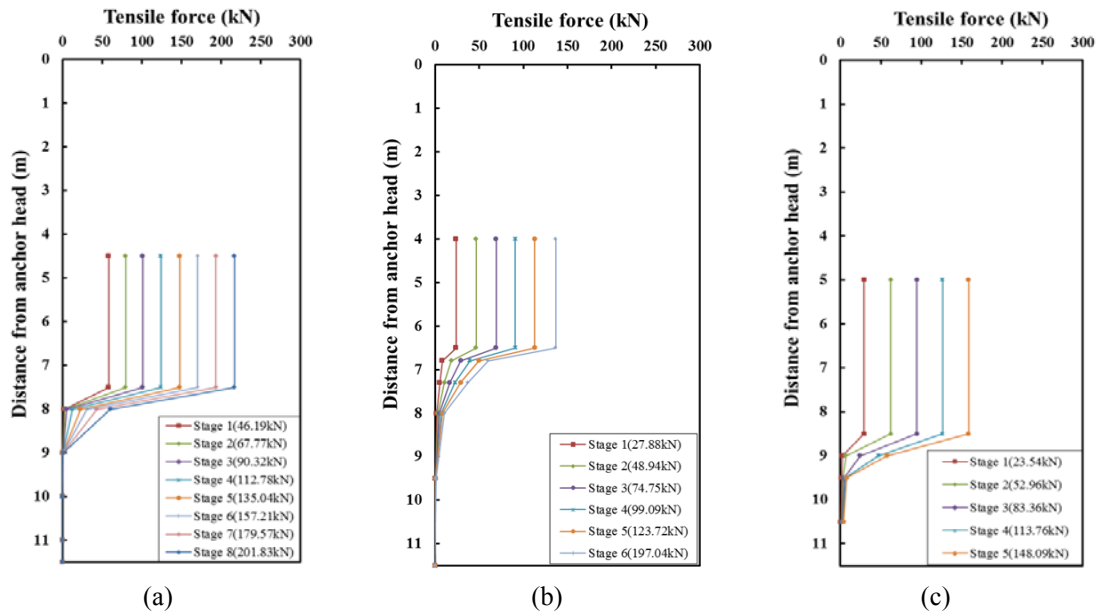


Fig. 11 Load transfer of anchors measured from FBG sensors: (a) anchor A₁; (b) anchor A₂; (c) anchor A₃

proximal section of the bonded part, gradually decreased, and almost dissipated at the distal section, at a depth of approximately 8 m. In the subsequent loading increments, there was a relative increase in the tensile force until the final loading stage of 201.83 kN. However, at the anchor depth of 9 m, there was no transfer of the prestress force even in the final loading stage. A load transfer depth of 1.5 m was visually observed for anchor A_1 .

Anchor A_2 was set up at the Yeosu site with the fixed parts surrounded by normal rock, and its load transfer distribution can be seen in Fig. 11(b). Interestingly, even though it was installed at a different ground condition, surrounded by normal rock, the tendencies of the prestress force transfer for all the loading stages, both in the free and fixed parts, were similar to the trends obtained for Anchor A_1 at the other Yeosu site. As expected, there were differences in the load transfer depths. The introduced prestress force of anchor A_2 transferred from 6.5 m to 9.5 m in depth, and the final load transfer depth was approximately 3 m.

Anchor A_3 was installed in a weaker ground condition at the Gimpo site, with the fixed parts surrounded by hard soil and approximately 1 m layer of weathered granite rock. The load transfer distribution for this anchor can be seen in Fig. 11(c). Again, even though Anchor A_3 was installed at the weaker ground condition, the distributions of the prestress force transfer for all the loading stages, in both the free and fixed parts, showed good agreement with the distributions obtained for the anchors at the Yeosu sites. However, because of the weaker ground condition, the bulk of the bond resistance migrated along almost the entire fixed length and reached near the distal end, especially in the final loading stages. In other words, the dissipative force points were fully transferred up to the distal end.

4. Numerical analyses and results

4.1 Modelling a pullout test anchor in laboratory

As mentioned before, a model rock body surrounding a grout column, in which the strand tendon was embedded, was prepared in the laboratory to replicate the installation conditions of the ground anchor. A static pullout test with the loading system was performed with six increments of load. In the current study, the finite difference analysis package FLAC 3D was used in the numerical analyses to study the load transfer mechanism of the ground anchor during the laboratory pullout test. Three governing materials, namely the strand tendon, grout, and assumed rock, were included in the FLAC 3D numerical simulation.

A total of 11200 zones and 12782 grid points were automatically generated in the finite difference grid. The bottom of the grid and the lateral boundaries were fixed. A relatively fine mesh was used near the grout–rock interface because large shear strain variations were expected, and the mesh became coarser with a ratio of 1.2 further away from the grout. The strand tendon was modeled as a cylindrical mesh with a diameter of 0.01524 m and a length of 0.9 m, whereas the grout was represented by a cylinder shell mesh surrounding the tendon with an outer diameter of 0.05 m and length the same as that of the tendon. The modeled rock diameter and length in the analysis were 0.3 m and 1 m, respectively, similar to the model rock in the laboratory. The 0.9 m long tendon was rested at the center of the 3D model from the top surface. The strand tendon was assumed to be installed in the normal rock condition, and the interface between the layers was incorporated with the same mechanical and material properties. Moreover, the rock was assumed to be homogeneous in the model. These assumptions were made to greatly reduce the complexity of the problem and the computation time but still maintain considerable accuracy. The material or

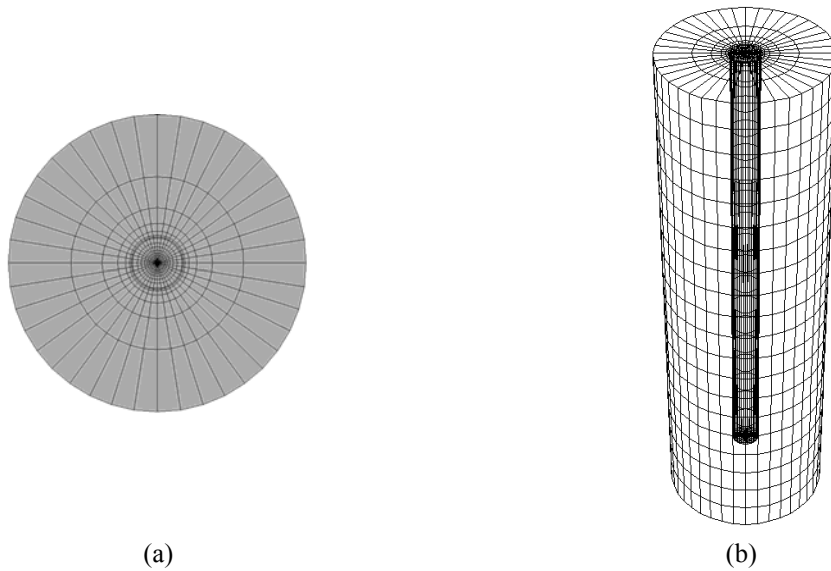


Fig. 12 3D finite difference grid used in the analyses FLAC 3D

constitutive model represents the deformation and strength behaviors prescribed to the different zones in a FLAC3D model. Several constitutive models are available in FLAC3D to simulate different types of behavior commonly associated with geologic materials, and the constitutive models and material properties can be assigned individually to every zone in the model. For this part of the study, an isotropic elastic model was used for the tendon, and the simplest and best-known criterion of failure, the Mohr–Coulomb criterion, which is controlled by a non-associated flow rule for shear failure and an associated rule for tension failure, was used for the rock and concrete zones. The material parameters used in the numerical analyses are detailed in Table 2.

Additionally, interface elements, which are connections between sub-grids that can separate (e.g., slide or open) during the calculation process and represent a physical discontinuity such as a fault, contact plane, or interface between two different materials, were utilized to allow relative displacement at the grout–rock and tendon–grout contact planes when yielding occurs. An interface element is defined by the normal stiffness and shear stiffness at a point in space near the contact with a finite plane, and they have the properties of friction, cohesion, normal stiffness, and shear stiffness. The values of the friction angle, normal stiffness, and shear stiffness govern the behavior of the interface.

Table 2 Material parameters used in numerical analyses for laboratory cases

Material	Model	Bulk modulus K (MPa)	Shear modulus G (MPa)	Unit weight γ (kN/m ³)	Poisson's ratio ν	Cohesion c' (kPa)	Internal friction angle ϕ' (°)
Grout	Mohr–Coulomb	14971.79	11228.84	20	0.2	2000	36
Concrete	Mohr–Coulomb	15229.83	12886.78	20	0.17	6000	39
Strand tendon	Elastic	166666.67	76923.08	78.5	0.3	-	-

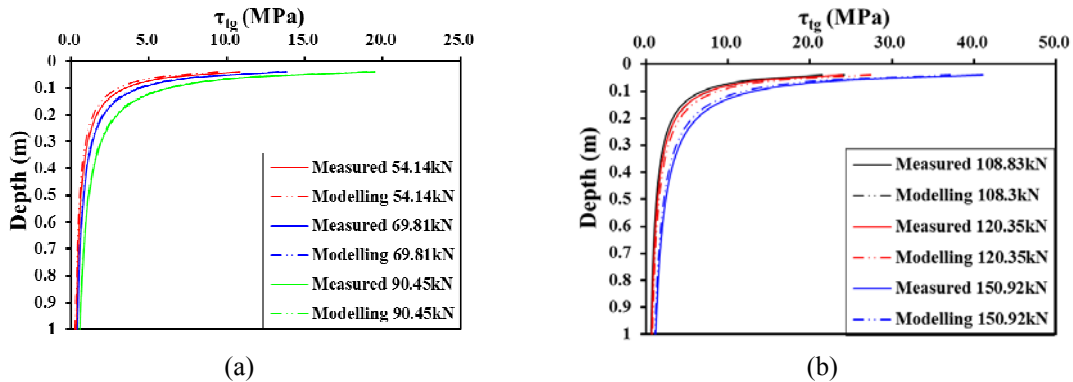


Fig. 13 Comparison of shear stress distribution at interface of tendon and grout: (a) Phase 1 (From loading stage 1 to loading stage 3); (b) Phase 2 (From loading stage 4 to loading stage 6)

In the numerical analysis, the modeling of the anchor load consisted of two stages, including initial geostatic equilibrium with a lateral earth pressure coefficient K_0 and the pullout loads at the top of anchor. The loads were sequentially applied up to the final design loading stage as follows:

- ▶ Stage 1: Applying the first pullout load $P_1 = 54.14$ kN by a normal stress of 296947 kPa on top of the anchor.
- ▶ Stage 2: Applying the second pullout load $P_2 = 69.81$ kN by adding a normal stress of 85947 kPa on top of the anchor.
- ▶ Stage 3: Applying the third pullout load $P_3 = 90.45$ kN by adding a normal stress of 113206 kPa on top of the anchor.
- ▶ Stage 4: Applying the fourth pullout load $P_4 = 108.83$ kN by adding a normal stress of 100811 kPa on top of the anchor.
- ▶ Stage 5: Applying the fifth pullout load $P_5 = 120.35$ kN by adding a normal stress of 63185 kPa on top of the anchor.
- ▶ Stage 6: Applying the sixth pullout load $P_6 = 150.92$ kN by adding a normal stress of 167670 kPa on top of the anchor.

The shear stress distribution at the tendon–grout interface measured by the two methods, FBG sensors embedded tendon and numerical modeling by FLAC 3D program, were compared for stages 1 and 2 with corresponding values of the introduced pullout loads, as shown in Figs. 13(a) and 13(b), respectively. The results were found to be consistent, not only in the trends but also in the fitted shear stress values. A comparison of typical shear stress distributions from experimental observation and numerical analysis is presented in Fig. 13.

4.2 Modeling in-situ pullout test anchor

As idealized in Fig. 14, the anchor was simulated as two parts, the free part and the fixed part. The cable–grout structural elements, available in the FLAC 3D program, were used to model the anchor, with all the properties for the free part assumed as zero. The cable elements simulating the anchor were modeled using the one-dimensional axial element in FLAC 3D. This element can be point-anchored or grouted to the surrounding material so that the cable element develops forces along its length as the surrounding media deform. It also can yield in tension or compression, but

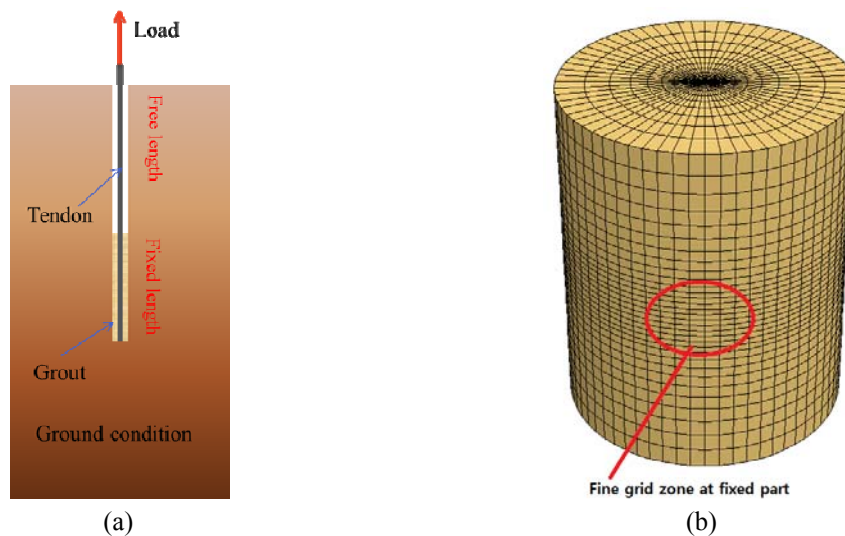


Fig. 14 Schematic idealization of ground anchor at field and 3D finite difference grid

cannot sustain a bending moment. Furthermore, a cable element can be initially pre-tensioned. With all of these suitable properties, the cable element was considered to be the best structural element for modeling the anchor. The cable-grout structure elements can be found in the studies of Wei and Cheng 2010; Lu 2012. At the fixed part, the shear behavior of the anchor–rock interface was modeled as cohesive and frictional. The shear behavior of the grout annulus during relative shear displacement between the cable–grout interface and the grout–rock interface was described numerically by the grout shear stiffness, grout cohesive strength, grout friction angle, grout exposed perimeter, and effective confining stress. Another key factor in this simulation was that the grout properties associated with each CableSEL were averaged at the cable nodes.

Fig. 14 shows the 3D finite difference grid used for modeling the anchors in the field. A fine grid zone was generated around the fixed part and near the grout–rock interface because of the probability of large shear strain variations. In total, 20480 zones, 21153 grid points, 23 structural elements, and 24 nodes were generated in the finite difference grid for each anchor. The bottom of the grid and the lateral boundaries were fixed. The same model dimensions of the finite difference meshes extending to a depth of 19 m below the ground surface and laterally to a distance of 8 m from the anchor centerline were applied for all anchors, with only differences in the soil stratum and their properties. The different soil layers were represented by different zone properties (Look 2007). The detailed material parameters of the soil layers at the sites used in the numerical analyses are detailed in Table 3. As in the anchor modeling for the laboratory pullout test, the simplest and best-known criterion of failure, the Mohr–Coulomb criterion, was used for all the soil layers simulated in the FLAC 3D program. Once the grid generation was complete, it was used for materials that yield when subjected to shear loading, but whose yield strengths depend on the major and minor principal stresses only; the intermediate principal stress has no effect on yield. As mentioned above, the cable element is the best structural element for modeling an anchor because of its advantageous properties. In these simulations, each cable structural element was defined by its geometric, material, and grout properties. A cableSEL is assumed to be a straight segment of uniform cross-sectional and material properties lying between two nodal points. Therefore, an

anchor can be modeled as a structure comprising a collection of cableSELS. The cableSEL behaves as an elastic, perfectly plastic material that can yield in tension and compression but cannot resist a bending moment. The cable was grouted such that a force develops along its length in response to relative motion between the cable and the grid, and grout properties were only applied to the fixed part. The grout behaves as an elastic, perfectly plastic material, with its peak strength being dependent on the confining stress and with no loss of strength after failure.

Table 3 Material parameters used in the numerical analyses for field cases

Rock type	Bulk modulus K (MPa)	Shear modulus G (MPa)	Poisson's ratio ν	Cohesion c' (kPa)	Internal friction angle ϕ' ($^\circ$)
Hard rock	15625	12711.86	0.18	4000	45
Normal rock	11111.11	8333.33	0.20	2000	40
Weathered granite rock	4938.27	3252.03	0.23	300	36
Weathered soil	50	23.08	0.3	50	30
Cover layer	44.12	16.92	0.33	30	29

Table 4 Applied pullout loads for each anchor

Anchor type	Applied loads(kN)							
	Stage1	Stage2	Stage3	Stage4	Stage5	Stage6	Stage7	Stage8
A ₁	46.19	67.77	90.32	112.78	135.04	157.21	179.57	201.83
A ₂	27.88	48.94	74.75	99.09	123.72	197.04	-	-
A ₃	23.54	52.96	83.36	113.76	148.09	-	-	-

For the field anchors, the applied load modeling also consisted of two stages, including initial geostatic equilibrium and the pullout loads at the top of the anchor. In the FLAC 3D program, a load can be applied to the first node of the cable structure, and the loaded node can be connected to the FLAC 3D grid or to another structural element immediately after the loading. At the fixed parts, the procedure used for subsequent "grouting" of the free length was to change the grout properties of the cableSELS comprising the free length to appropriate values for a grouted section. In the simulations, each anchor had a different applied pullout load system sequentially applied until the final design loading stage, as detailed in Table 4.

Figs. 15(a), (b) and (c) compare the tensile distributions along the tendon from the two methods, numerical computation using the FLAC 3D program and measurement method using FBG sensors, for anchors A₁, A₂, and A₃, respectively. The field test and numerical results were compared not only to investigate the feasibility of using FBG sensors for monitoring the load transfer mechanism of anchors but also to visualize the load transfer distribution by numerical simulations in cases of difficulties in in-situ measurements. All the results with respect to the load increments were consistent between the two proposed methods, not only in trend but also in magnitude. They showed more consistency at the high pullout loading stages compared with the lower ones, especially at the final loading stage for each anchor. Because the measurements in the field tests using the FBG sensors were only made at certain points along the anchors, the load transfer distribution had to be predicted based on these values. Thus, the deviations between the two methods are only exposed at some local points.

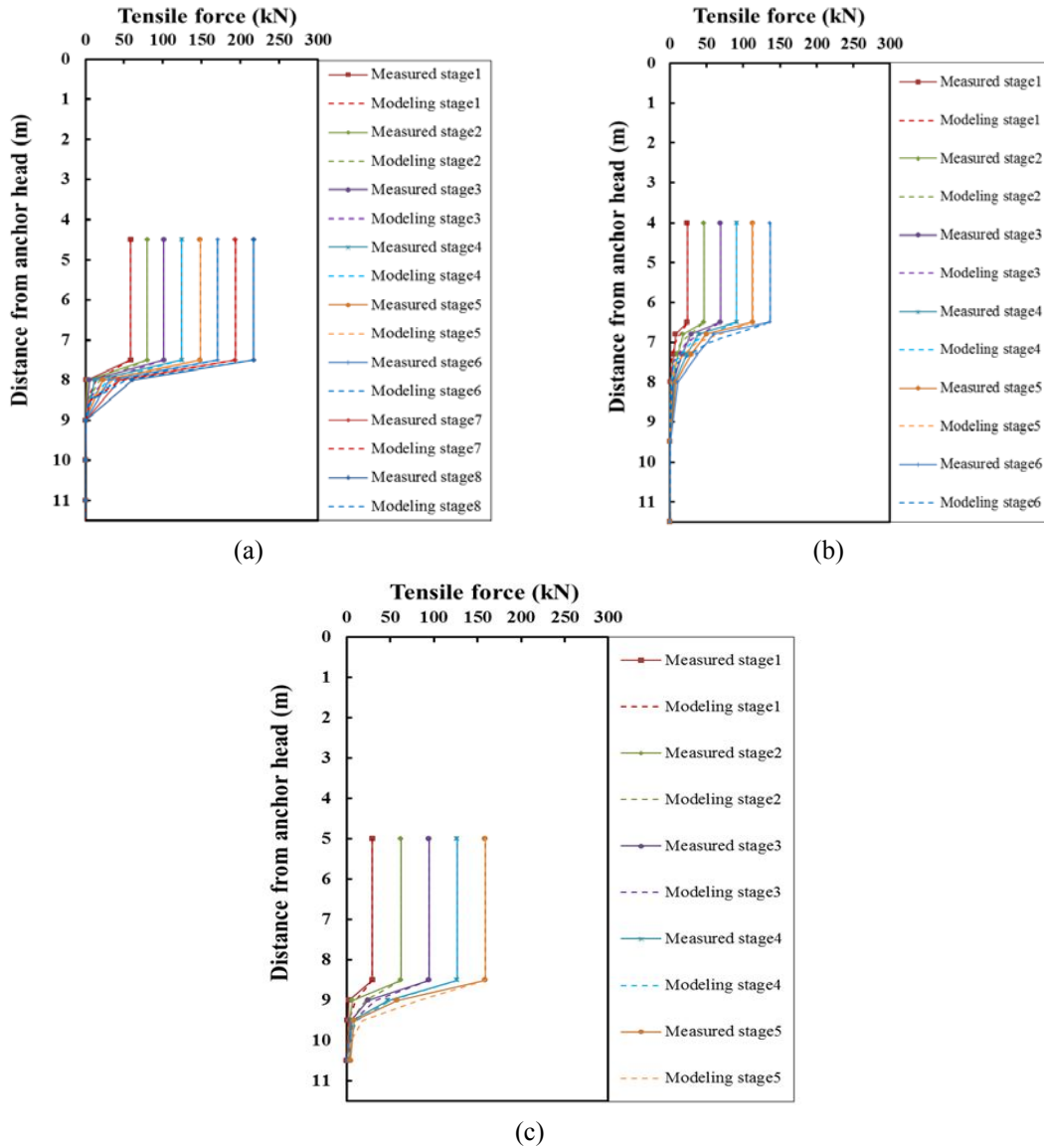


Fig. 15 Comparison of tensile force distribution along tendon of anchors: (a) Anchor A₁; (b) Anchor A₂; (c) Anchor A₃

In addition, the comparison of results from the two methods provided clear evidence regarding the dependency of the load transfer depth on the ground condition surrounding the fixed parts of the anchor. The load transfer depth was short, approximately 1.5 m, in the hard rock condition at the first Yeosu site, whereas it was longer, approximately 3 m, in the normal rock condition at the second Yeosu site. For the anchor installed at the Gimpo site, the bulk of its bond resistance was transmitted almost along the entire fixed length and nearly reached the distal end, especially in the final loading stage. In other words, the dissipative force points were almost transferred up to the distal end.

5. Suggestions for anchor design based on numerical analysis

As verified above, there is an interactive relationship between the load transfer depth of an anchor and its surrounding ground conditions. In order to thoroughly understand this relationship, different constitutive models for various surrounding ground conditions, namely very hard rock, hard rock, normal rock, moderately weak rock, weak rock, weathered rock, and hard soil, were analyzed using the finite difference program (FDM) FLAC 3D. The detailed properties of the soil layers surrounding the bonded part used in the numerical analyses are detailed in Table 5.

It is worth noting that the load transfer depth varies with the soil condition, being shorter in hard ground conditions and longer in weaker ones. This relationship can be clearly observed from the estimated load transfer depth chart obtained by numerical analysis, as shown in Fig. 16. For anchor design, the load transfer depth is a key parameter for satisfying implicit economic criteria and should be appropriately determined. In this part of the study, finite difference results of 91 cases were used for a multi-regression statistical analysis to develop an equation for estimating the optimal load transfer depth that can facilitate efficient anchor design.

Table 5 Parameters of surrounding ground conditions used in numerical analyses

Material	E (MPa)	ν	c' (kPa)	ϕ ($^{\circ}$)
Cherokee marble	55800	0.18	10000	48
Bedford limestone	28500	0.2	5000	42
Micaceous shale	11100	0.22	1000	38
Sandy shale	8000	0.25	800	36
Weak rock	4000	0.25	400	34
Weathered rock	1000	0.26	300	32
Hard soil	500	0.3	150	30

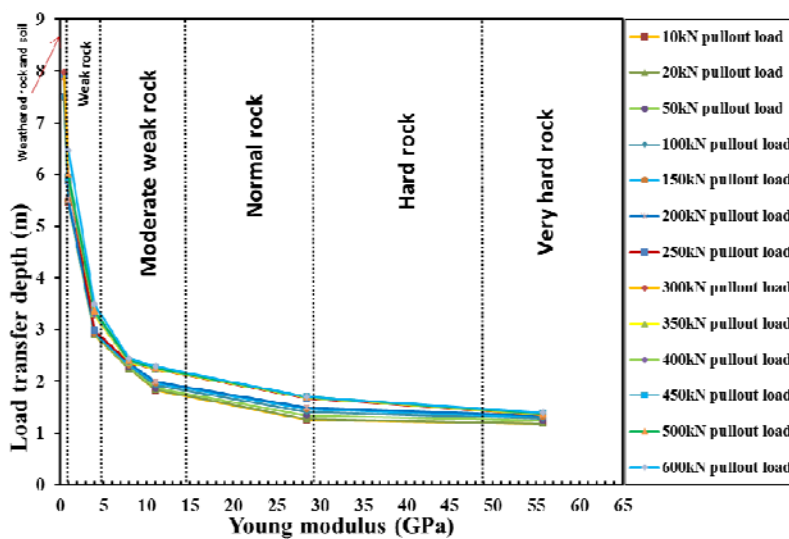


Fig. 16 Load transfer depth estimation from numerical analysis

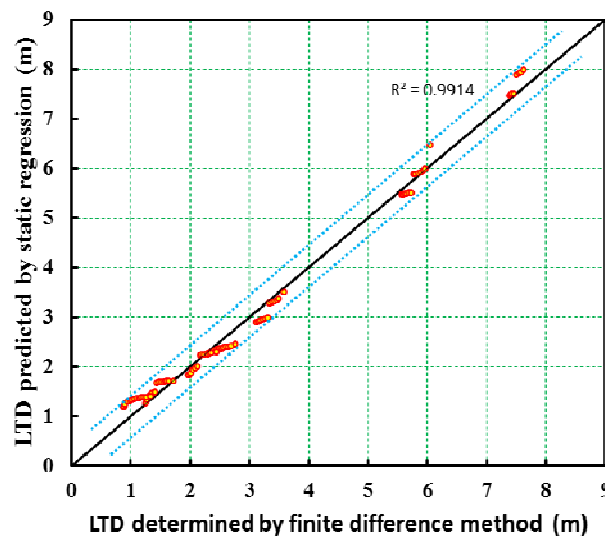


Fig. 17 Comparison between the *LTD* calculated from FDM and *LTD* predicted from statistic regression

The regression *LTD* in Eq. (3) was further verified by comparing the results of the regression model with those from 91 finite difference analysis cases. The comparison between the *LTD* calculated from FDM and the *LTD* predicted from statistic regression are graphically illustrated in Fig. 17, which shows a good match between the values. In addition, the high R-squared value of 0.9914 suggests that the load transfer depth equation has acceptable accuracy.

6. Conclusions

In this study, experimental and numerical studies were conducted to investigate the load transfer mechanism and load transfer depth of ground anchors based on a series of laboratory and field load tests. Optical FBG sensors embedded in the central king cable of a seven-wire strand were employed to monitor the changes in the tensile force and its distribution along the tendons. The laboratory and in-situ load test results were compared with equivalent case studies simulated using the finite difference method in the FLAC 3D program. The following conclusions were drawn:

- First, the accuracy of strain measurement using fiber optic sensors was verified. After good agreement was found with the measurement of strain gauges attached outside the tendon, the FBG sensors were employed to investigate the load transfer mechanism of the model anchor in the laboratory test. The use of FBG sensors in monitoring strains shows great potential for accurate analysis of anchor load transfer.
- For the in-situ experiments, tension-type anchors were installed in various ground conditions, such as weathered granite soil, weathered rock, normal rock, and hard rock, for the verification of a tension-force monitoring of ground anchors at actual sites. The results of the in-situ pullout tests demonstrated that the proposed tendon embedded with the FBG sensors could be practically applicable to ground anchors, as the short-term tension force measurement values were close to those obtained by a delicate load cell installed at the

anchor head. The prestress force and the load transfer phenomenon due to the introduction of the prestress were clearly visualized. With the FBG sensors installed at the free and fixed parts, the instantaneous monitoring of the prestress force and load transfer phenomenon was successfully achieved. Based on these test results, the proposed smart tendon embedded with FBG sensors is projected to be an alternative monitoring tool for prestress force measurement at the introduction stage and long-term health monitoring of the ground anchor.

- It was verified that dimensional parametric numerical analyses using the FLAC 3D program could efficiently simulate the model pullout test anchor in the laboratory, with accurate prediction of load transfer distributions. Moreover, the comparison of results from the laboratory test and the numerical simulation corroborated the changes in load transfer mechanism with the increase in the introduced prestress force as well as the increase in load transfer depth with the loading increments.
- The observed measurements from the in-situ load tests were compared with equivalent case studies simulated using the finite difference method in the FLAC 3D program. All the results obtained from the two proposed methods were found to be consistent with respect to the load increments. They were close to each other not only in trend but also in magnitude and showed more consistency at higher pullout loading stages, especially at the final loading stage of each anchor. The load transfer distribution had to be predicted based in these values. Thus, the deviations between the two methods were only exposed at some local points. The field test and numerical simulation results were compared not only to investigate the feasibility of using FBG sensors for monitoring the load transfer mechanism of anchors but also to visualize the load transfer distribution using the numerical method in cases of difficulties in in-situ measurements.
- Finally, in both the proposed methods demonstrated the pronounced dependency of the load transfer depth on the surrounding ground conditions, the load transfer depth was shorter in hard ground conditions and longer in weaker ones. Considering the safety factor FOS , the bonded length of the anchor can be simply expressed as follows:

$$L_{bonded\ length} = FOS \times (6.0 \times E^{-0.381} + 0.793 \times P - 0.426)$$

Acknowledgments

This research was supported by a grant (15RDRP-B076564-02) from Regional Development Research Program funded by Ministry of Land, Infrastructure and Transport of Korean.

References

- Aliciuc, C.L. and Musat, V. (2013), "Identification of soil models by simulation of ground anchor tests, using FEM", *Buletinul Institutului Politehnic din Iasi. Sectia Constructii, Arhitectura*, **59**(4), 145 p.
- Aydan, O., Ebisu, S. and Komura, S. (1993), "Pull-out tests of rock anchors and their failure modes", *Proceedings of the International Symposium on Assessment and Prevention of Failure Phenomena in Rock Engineering*, Istanbul, Turkey, April, pp. 285-293.
- Aydan, O., Komura, S., Ebisu, S. and Kawamoto, T. (1995), "A unified design method for anchor foundations of super-high pylons", *Proceedings of the International Workshop on Rock Foundation*, Tokyo, Japan, September.

- Benmokrane, B., Chekired, M. and Xu, H. (1995), "Monitoring behavior of grouted anchors using vibrating-wire gauges", *J. Geotech. Eng.*, **121**(6), 466-475.
- Chang, D.W., Cheng, S.H. and Lee, W.-F. (2008), "Simulation and interpretation of ground anchor failures from acoustic monitoring test", *Proceedings of the 3rd Taiwan-Japan Joint Workshop on Geotechnical Natural Hazards*, Keelung, Taiwan, October.
- Cornelia, S.H., Tilmann, S., Marcel, N., Gnter, B., Robert, L., Christoph, B. and Wolfgang, S. (2003), "Strain measurements by fiber Bragg grating sensors for in situ pile loading tests", *Proceedings of the SPIE 5050*, San Diego, CA, USA, March.
- Farmer, I.W. (1975), "Stress distribution along a resin grouted rock anchor", *Int. J. Rock Mech. Min. Sci. Geomech. Abstr.*, **12**(11), 347-351.
- Gupta, B.D. (2006), *Fiber Optic Sensors: Principles and Applications*, New India Publishing, New Delhi, ND, India.
- Itasca Consulting Group (2006), *FLAC 3D Fast Lagrangian Analysis of Continua User's and Theory Manuals*, Minneapolis, MN, USA.
- Ivanovic, A. and Neilson, R.D. (2009), "Modelling of debonding along the fixed anchor length", *Int. J. Rock Mech. Min. Sci.*, **46**(4), 699-707.
- Kesavan, K., Ravisankar, K., Parivallal, S. and Sreeshylam, P. (2005), "Applications of fiber optic sensors for structural health monitoring", *Smart Struct. Syst., Int. J.*, **1**(4), 355-368.
- Kim, J.M., Kim, Y.S., Kim, H.W., Seo, D.N. and Yun, C.B. (2007a), "Development of smart tendon instrumented with optical FBG sensors", *J. Computat. Struct. Eng. Inst. Korea*, **20**(2), 121.
- Kim, N.K., Park, J.S. and Kim, S.K. (2007b), "Numerical simulation of ground anchors", *Comput. Geotech.*, **34**(6), 498-507.
- Kim, Y.S., Seo, D.N. and Kim, J.M. (2008), "Development and application of a smart anchor with optical FBG sensors", *Proceedings of KGS Spring National Conference 2008*, Seoul, Korea, March, pp. 393-398.
- Kim, Y.S., Seo, D.N., Kim, J.M. and Sung, H.J. (2009), "Load Transfer Characteristics of the 7-wire strand using FBG Sensor Embedded Smart Tendon", *J. Korea Soc. Hazard Mitig.*, **9**(5), 79-86.
- Kim, Y.S., Sung, H.J., Kim, H.W. and Kim, J.M. (2011), "Monitoring of tension force and load transfer of ground anchor by using optical FBG sensors embedded tendon", *Smart Struct. Syst., Int. J.*, **7**(4), 303-317.
- Kim, Y.S., Do, T.M. and Jung, S.H. (2013), "Modelling of load transfer measured from smart tendon embedded ground anchors with finite difference method", *Proceedings of KSCE Conference 2013*, Seoul, Korea, June, pp. 969-972.
- Lee, W.J., Lee, W.J., Lee, S.B. and Salgado, R. (2004), "Measurement of pile load transfer using the Fiber Bragg Grating sensor system", *Can. Geotech. J.*, **41**(6), 1222-1232.
- Look, B. (2007), *Handbook of Geotechnical Investigation and Design Tables*, Taylor & Francis/Balkema, Netherlands.
- Lu, D.H. (2012), "Numerical approach for the mechanical behavior of fully grouted anchorage system subjected to pullout test", *Electron. J. Geotech. Eng.*, **17**, 531-543.
- Moerman, W., Taerwe, L., Waele, W.D., Degrieck, J. and Himpe, J. (2005), "Measuring ground anchor forces of a quay wall with bragg sensors", *J. Struct. Eng.-ASCE*, **131**(2), 322-328.
- Schroeck, M., Ecke, W. and Graupner, A. (2000), "Strain monitoring in steel rock bolts using FBG sensor arrays", *Proceedings of the SPIE 4074*, Glasgow, United Kingdom, May.
- Shields, D.R., Schnabel, H. and Weatherby, D.E. (1978), "Load transfer in pressure injected anchors", *J. Geotech. Eng. Div.*, **104**(9), 1183-1196.
- Wei, W.B. and Cheng, Y.M. (2010), "Soil nailed slope by strength reduction and limit equilibrium method", *J. Comput. Geotech.*, **37**(5), 602-618.
- Xanthakos, P.P. (1991), *Ground Anchor and Anchored Structures*, A Wiley- Inter-Science Publication.